Ocean loading effects on stress at near shore plate boundary fault systems

Karen Luttrell[1] and David Sandwell[1]

Received 14 April 2009; revised 8 March 2010; accepted 6 April 2010; published 26 August 2010.

[1] Changes in eustatic sea level since the Last Glacial Maximum create a differential load across coastlines globally. The resulting plate bending in response to this load alters the state of stress within the lithosphere within a half flexural wavelength of the coast. We calculate the perturbation to the total stress tensor due to ocean loading in coastal regions. Our stress calculation is fully 3-D and makes use of a semianalytic model to efficiently calculate stresses within a thick elastic plate overlying a viscoelastic or fluid half-space. The 3-D stress perturbation is resolved into normal and shear stresses on plate boundary fault planes of known orientation so that Coulomb stress perturbations can be calculated. In the absence of complete paleoseismic indicators that span the time since the Last Glacial Maximum, we investigate the possibility that the seismic cycle of coastal plate boundary faults was affected by stress perturbations due to the change in sea level. Coulomb stress on onshore transform faults, such as the San Andreas and Alpine faults, is increased by up to 1–1.5 MPa, respectively, promoting failure primarily through a reduction in normal stress. These stress perturbations may perceptibly alter the seismic cycle of major plate boundary faults, but such effects are more likely to be observed on nearby secondary faults with a lower tectonic stress accumulation rate. In the specific instance of rapid sea level rise at the Black Sea, the seismic cycle of the nearby North Anatolian fault was likely significantly advanced.

Citation: Luttrell, K., and D. Sandwell (2010), Ocean loading effects on stress at near shore plate boundary fault systems, *J. Geophys. Res.*, *115*, B08411, doi:10.1029/2009JB006541.

1. Introduction

[2] Global mean (eustatic) sea level is temporally subject to many processes. The largest is the Milankovitch cycle whereby water mass is periodically transferred between the global ocean (high sea level) and solid ice buildup at the poles (low sea level). The Last Glacial Maximum (LGM) ended about 21 ka, and since that time, eustatic sea level has risen ~120 m [*Peltier*, 2004; *Peltier and Fairbanks*, 2006] at a rate of up to 1.25 cm/yr, reaching its approximate current level 4 ka (Figure 1). As sea level rose, the extra water acted as an additional vertical load to the ocean basins but not to the continents. In response to this uneven load, the lithosphere at all coastlines globally flexed about the edge of the load at the shoreline.

[3] Many previous studies have focused on the subsidence of ocean basins in response to sea level rise as a way of constraining rheologic models of earth structure [e.g., *Lambeck and Chappell*, 2001; *Lambeck et al.*, 2002a; *Peltier and Drummond*, 2008], but these analyses are not repeated here. Instead, this study focuses on the stresses induced in the near shore lithosphere as it flexes about coastlines globally. These flexure-induced stresses cause a perturbation to the total stress state in the lithosphere within half a flexural wavelength of the coast, both offshore and onshore (Figure 2).

[4] It is possible that the change in the lithospheric stress state from ocean loading-induced flexure impacted the ongoing tectonic processes in coastal regions, particularly where the coastal region overlaps a plate boundary or other feature of geophysical interest. It is therefore the principal aim of this study to investigate the potential impact to plate boundary processes, particularly the shear faulting cycle, from the perturbing stress from sea level rise since the LGM. If we assume this stress perturbation is independent of other sources of stress in a region, we may make this determination by calculating the stress of a flexing thick plate resolved onto a particular fault plane.

[5] Estimates of fault slip rate from geologic and geodetic methods show consistent discrepancies [e.g., *Bennett et al.*, 2004; *Matmon et al.*, 2005]. Several studies have addressed this discrepancy by adjusting either the geologic or geodetic rate with the hope of reconciling the two numbers [e.g., *Bennett et al.*, 2004; *Hetland and Hager*, 2006; *Oskin et al.*, 2007]. Other studies, however, have suggested that the difference in the geologic and geodetic estimates of fault slip rate may be revealing subtle details of the long-term faulting process [e.g., *Chery and Vernant*, 2006; *Dolan et al.*, 2007; *Hampel and Hetzel*, 2006; *Hetzel and Hampel*, 2005; *Luttrell et al.*, 2007]. If the stress perturbations from ocean loading

[1]Scripps Institution of Oceanography, La Jolla, California, USA.

0148-0227/10/2009JB006541

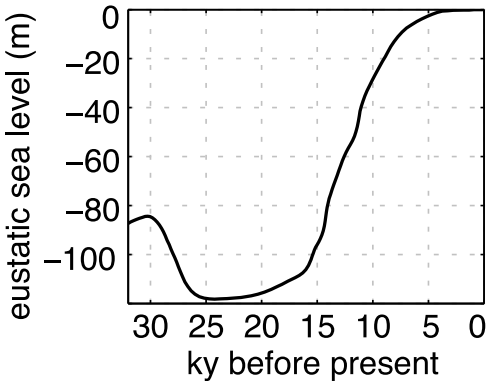

Figure 1. Eustatic sea level since the Last Glacial Maximum relative to present day level [*Peltier and Fairbanks*, 2006].

throughout the Milankovich cycle are large enough, they may influence the seismic cycle of coastal faults sufficiently that the slip rate and recurrence interval of earthquakes on those faults would be perceptibly altered. This would be an example of a physical process external to the seismic cycle affecting the faulting process. There are not currently many paleoseismic indicators that sufficiently span the time since the LGM in a way that would allow these predictions to be rigorously tested, though a few studies do offer some observations of long-term fault behavior [e.g., *Rockwell et al.*, 2009]. We therefore present a model-based analysis of the stress changes ocean loading is likely to create and the impact such perturbations would have on observable paleoseismic indicators, so as to better understand the influence sea level rise may have on long-term plate boundary behavior.

[6] Several studies have addressed the response of the earth to surface loads of water that come and go over various time scales and investigated their role in seismic triggering. The seasonal response to meters of precipitation in Japan and the Himalayas alters stress by a few kilopascals and has been shown to affect seismicity rate [*Bettinelli et al.*, 2008; *Bollinger et al.*, 2007; *Heki*, 2001; *Heki*, 2003]. The filling of new reservoirs with tens of meters of water can trigger seismicity not only from the immediate elastic response but also from the temporal flow of pore fluids in the crust, which may perturb stress by a few tens of kilopascals for several years after filling [e.g., *Gahalaut et al.*, 2007; *Simpson et al.*, 1988]. In a few cases, hundreds of meters of water removed as entire lakes empty affect stresses both by altering the pore pressure in the crust and inducing flexure in the lithosphere. These changes alter stress by a few megapascals over thousands of years [*Hampel and Hetzel*, 2006; *Hetzel and Hampel*, 2005] or a few hundred kilopascals over hundreds of years [*Luttrell et al.*, 2007] and can affect the slip rate of nearby faults. On the largest and longest scale, glacial rebound following the removal of kilometers of ice may alter stresses tens of megapascals for many thousand years following unloading and can reactivate seismicity on previously dormant faults [e.g., *Grollimund and Zoback*, 2000; *Ivins et al.*, 2003; *Johnston et al.*, 1998]. Additionally, there have been numerous investigations of regional subsidence and flexure associated with sea level rise that have not calculated the perturbing contribution to the stress state [e.g., *Ivins et al.*, 2007; *Kendall et al.*, 2003; *Lambeck and Purcell*, 2005]. The load considered in this study acts over the same time period as polar ice cap melting, but it has smaller amplitude and is more widespread since the change in sea level is global. The largest flexure-induced stresses are present only within a flexural wavelength of the coastline, generally a few hundred kilometers. For this reason, our analysis more closely resembles the cases of local lake unloading than widespread glacial rebound.

[7] In the sections that follow, we develop the model used to calculate bending stress from ocean loading globally and the method of resolving this into Coulomb stress on a particular fault plane. We then more closely examine the stress predictions at two coastal transform boundaries (San Andreas fault and Alpine fault) and a near shore subduction boundary (Cascadia subduction zone). We also examine a special instance of ocean loading stress on a coastal transform in response to a very rapid sea level rise (North Anatolian fault).

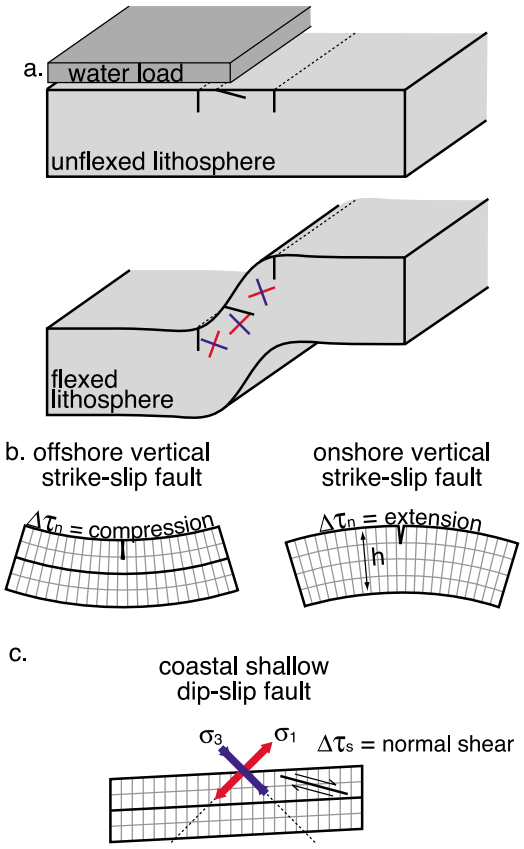

Figure 2. (a) Schematic of thick plate flexure about coastline due to an ocean load. Red and blue bars show direction of maximum (extension) and minimum (compression) principal stresses from flexure about coastline. The short black lines show the location of an onshore and offshore vertical fault as well as a near shore shallow dipping fault, and the dotted lines represent the surface trace of these faults. Ocean loading will perturb stress on an offshore or onshore (b) vertical strike-slip fault differently from a (c) shallow-dipping coastal dip-slip fault. For vertical strike-slip faults, the normal stress component is dominant. For a shallow dipping dip-slip fault, the shear stress component may also play a role.

Finally, we discuss the implications of our calculations for the understanding of long-term fault behavior.

2. Methods

2.1. Plate Bending Stress From Ocean Loading

[8] The stress perturbation from ocean loading is just one component of the total stress tensor in a region. In addition to the lithostatic stress that increases with depth and remains constant over time, a region is also subject to the broad tectonic stress that drives plate motions and changes over geologic timescales (10^6 years). The ocean loading component we calculate changes on the timescale of the Milankovitch cycles (10^4–10^5 years). Local stresses associated with the earthquake cycle of a particular fault evolve over the timescale of the recurrence interval of that fault (10^2–10^4 years). Because all of these sources of stress act over very different timescales, we can calculate their effects independently from one another and add them linearly to get the total stress σ_{ij}, as seen below

$$\sigma_{ij} = (\rho g z)\mathbf{I}_{ij} + \tau_{ij}^{\text{tectonic}} + \tau_{ij}^{\text{ocean loading}} + \tau_{ij}^{\text{faults}}, \qquad (1)$$

where ρ is the density, g is gravity, z is the vertical coordinate, $\mathbf{I}_{ij}$ is the identity matrix, and τ_{ij} represents a stress deviation from the lithostatic state from various sources. We can therefore calculate the effect of stress change from ocean loading $\Delta\tau_{ij}^{\text{ocean loading}}$ on the total stress $\Delta\sigma_{ij}$ without needing to specify forms for the regional tectonic or local earthquake cycle stresses (hereafter, we shall refer to stress perturbation from ocean loading as $\Delta\tau_{ij}$). This is only possible because the ocean loading strains are small so we can assume a linear stress-strain relationship.

[9] We model stress perturbations from ocean loading by first calculating the full 3-D stress tensor from a vertical surface load in a thick elastic plate overlying a Maxwell viscoelastic half-space. The plate is both uniformly thick and uniformly strong. We make no assumptions about the orientations of the principal axes of the stress tensor, nor do we assume any of the six Cartesian stress components are zero, particularly $\tau_{xz} \neq \tau_{yz} \neq 0$. The calculations are done using a semianalytic Fourier model [*Luttrell et al.*, 2007; *Smith and Sandwell*, 2004] such that vertical displacements and derivatives are calculated from analytic solutions and horizontal displacements and derivatives are calculated in the Fourier domain (see Appendix A for a summary of model details). This is equivalent to calculating the analytic Green's function response to a point load and then convolving that response with the true 2-D shape of the load. The semianalytic model is advantageous because use of the 2-D fast Fourier transform allows fast model calculations with true load geometry. However, the rheologic vertical stratification is necessarily simple to allow an analytic vertical solution. Also, the horizontal wavelength of the load distribution is numerically restricted to be less than the width of the grid used for computation. This model has previously been benchmarked against known analytic solutions [see *Luttrell et al.*, 2007].

[10] For the model input, we use a eustatic sea level curve since the LGM that takes into account multiple local data sets from around the world as well as a model of isostasy to account for changes in basin volume as the lithosphere flexes under the weight of the water (Figure 1) [*Peltier*, 2004; *Peltier and Fairbanks*, 2006]. The bathymetry of the seafloor is determined from the new SRTM30_PLUS global topography/bathymetry grid [*Becker et al.*, 2009], which is particularly accurate in shallow coastal areas (depth < 300m) where ship soundings are abundant. The true load geometry, therefore, is known exactly. This exact load shape is input into our model without simplification, accounting for the migration of the shoreline as sea level rises.

[11] As previously mentioned, the assumption that these stress components add linearly to the regional background state of stress (equation 1) allows us to study the stress perturbations induced by ocean loading without having to specify anything about the other sources of stress present in a region. We are primarily interested in the change in stress over time not the absolute stress state itself. Therefore, we generally take the initial stress to be that at the time of the LGM, though this choice is of course arbitrary and we could equally examine any time period of interest.

[12] For the elastic plate, we assume a Young's modulus of 70 GPa and a Poisson's ratio of 0.25. The only two model parameters to consider are the thickness of the elastically strong plate h and the viscosity of the underlying half-space η. However, because the eustatic sea level rise is so gradual, any time delay in the flexural response due to the viscous asthenosphere would be negligible for a viscosity of 10^{20} Pa s or less (corresponding to a Maxwell relaxation time of about 200 years). The asthenosphere viscosity in a plate boundary region is typically less than 10^{20} Pa s by as much as 2 orders of magnitude [e.g., *James et al.*, 2000; *Lambeck and Purcell*, 2005]. In general, therefore, we examine the fully relaxed response, equivalent to an elastic plate over a fluid half-space. (A special case of rapid ocean loading is treated in section 3.3.)

[13] The choice of plate thickness is important because h affects the flexural rigidity and flexural wavelength. Consequently, a thicker bending plate will affect a larger area around the coastline, whereas stresses in a thinner plate will be more localized. Global post-glacial rebound studies generally suggest a plate 65 km or thicker is appropriate for continents and a 50 km thick plate is appropriate for ocean basins [e.g., *Lambeck and Chappell*, 2001; *Lambeck et al.*, 2002b], but along tectonically active coastal margins, a thinner plate of 40 km or less may be more appropriate [e.g., *James et al.*, 2000]. For the purposes of this study, we examine stress perturbations in a plate of intermediate thickness, $h = 50$ km, corresponding to a flexural wavelength about 500 km. The magnitude of the stress perturbations also depends on the depth of observation within the plate relative to the plate thickness (z/h), with larger bending stresses near the surface and smaller stresses closer to the center of the plate (see Appendix A). We choose an observation depth of 10 km, which is a typical seismogenic depth on the transform faults considered here and is approximately the depth of the base of the elastic zone of the Cascadia subduction zone [*Fluck et al.*, 1997].

[14] The extent to which a fault in a coastal region is affected by plate bending stresses from ocean loading depends not only on the thickness of the flexing plate, as mentioned above, but also on the shape of the coastline and the location of the boundary. We calculated the fully relaxed global stress perturbation in a 50 km thick plate due to 120 m of sea level rise, using the exact shape of the ocean basin

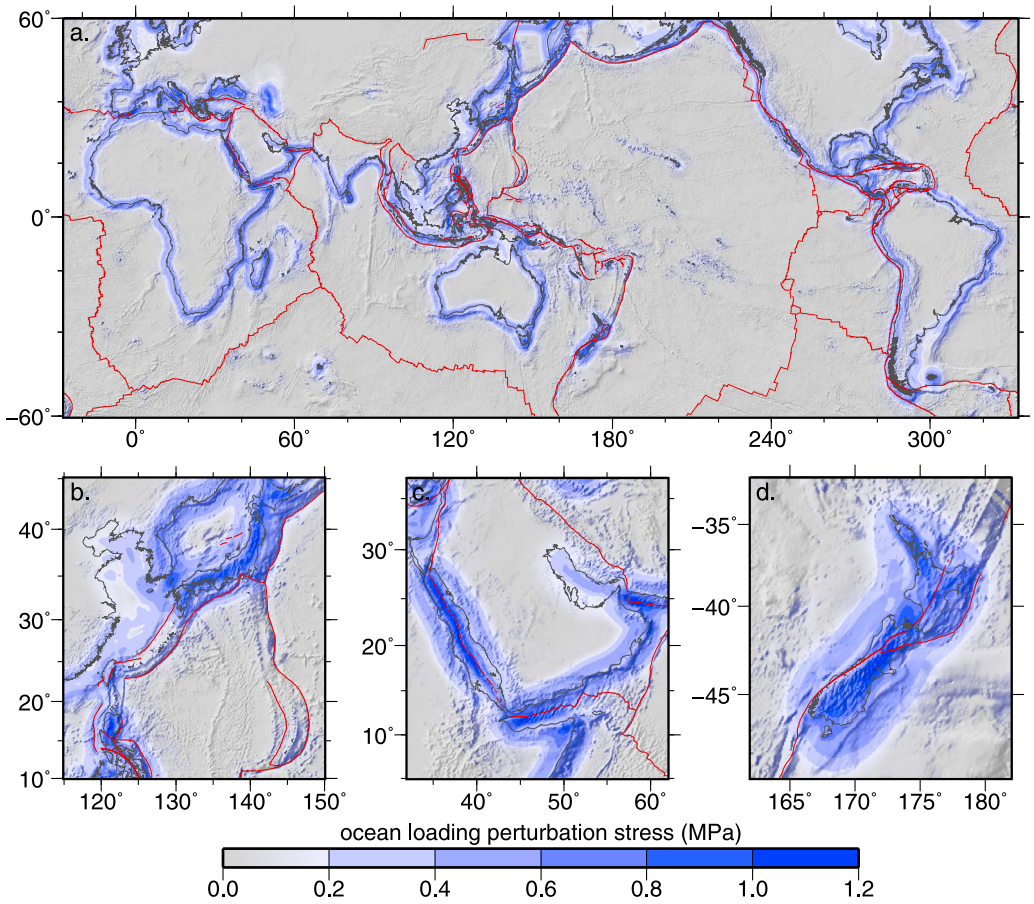

Figure 3. (a) Maximum shear stress perturbation from ocean loading on a 50 km thick plate. Optimally oriented faults could experience up to a 1.2 MPa change in shear stress at all coastlines globally in addition to a pressure change of similar magnitude. Tectonic plate boundaries (red) in coastal regions may be affected by the stress perturbations. (b) Deep sea subduction zones will not be affected by ocean loading, but near-land subduction zones may be affected depending on their proximity to the coast. (c) In narrow gulfs where the width of the water load is close to half the flexural wavelength, bending stress magnitude may be higher. (d) Loading on multiple sides of a narrow landmass of width close to half the flexural wavelength also concentrates the bending stress, resulting in higher magnitudes.

without any simplification of the coastline. The maximum shear stress, $(\sigma_1 - \sigma_3)/2$, where σ_1 and σ_3 are the maximum and minimum principal stresses, is shown in Figure 3 and gives an idea of the "size" of the stress perturbation, allowing a simple comparison of the effects of geography. The areas of greatest potential stress perturbation are within a few hundred kilometers of the coast, both on- and offshore [*Kendall et al.*, 2003], where an optimally oriented fault could experience a 1.2 MPa change in shear stress in addition to a pressure change of similar magnitude. Anywhere a tectonic plate boundary (shown as red lines) coincides with a coastline, there is the potential for the faults associated with that boundary to be influenced by the rise in sea level. Far offshore features like mid-ocean ridges and deep ocean subduction zones are unaffected by ocean loading (Figure 3b) because the ocean load is uniform there and no bending stresses are induced. A coastal subduction zone may or may not be affected depending on its proximity to the coast. An onshore transform fault, however, such as the San Andreas, North Anatolian, or Alpine fault, is well positioned to experience large stress perturbations from ocean loading.

[15] Bending stresses from ocean loading are particularly pronounced in regions where the narrow strips of water or land have a width equal to about half the flexural wavelength. In these cases, the geometry of the load concentrates the stress of bending. This is the case at the Red Sea (Figure 3c), where the 250 km width of the gulf happens to correspond to the half flexural wavelength of a 50 km thick plate, making the maximum shear stress there larger than it is a comparable distance offshore in the open ocean. This stress concentration is less pronounced, however, when a thinner plate is used to calculate bending stresses, which is likely more appropriate in a rifting zone. Similarly, stress on a narrow strip of land such as the islands of New Zealand or Japan may be as much as 50% larger than stress a comparable distance inland from a continental coastline if their width is similar to the half flexural wavelength (Figure 3d). Again, however, this stress concentration phenomenon is sensitive to the choice of model plate thickness. Though the coastal stresses from ocean loading are present globally, we shall focus in this study on the San Andreas fault (SAF), Alpine fault, North Anatolian fault (NAF), and Cascadia subduction zone (CSZ) systems as

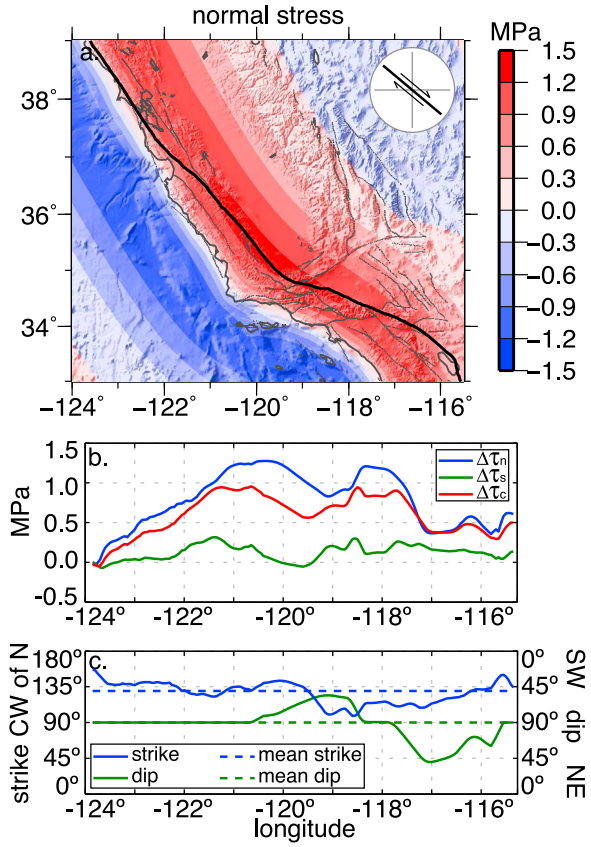

Figure 4. (a) San Andreas region ocean loading perturbation to normal stress resolved on a vertical plane striking 50°W of north. Actual SAF trace shown (thick black line). Positive and negative normal stresses represent extensional and compressional perturbations, respectively. (b) Normal (blue), shear (green), and Coulomb stress (red) resolved onto the actual SAF plane with varying orientation (c) along its length.

representatives of major transform and subduction boundaries under different loading conditions.

2.2. Ocean Loading Stress on Plate Boundary Faults

[16] We use the above model to calculate the perturbation to the six components of the 3-D Cartesian stress tensor $\Delta\tau_{ij}$. We interpret the 3-D change in stress by calculating differential Coulomb stress resolved on a fault plane of known orientation $\Delta\tau_c$ [e.g., *King and Cocco*, 2001; *King et al.*, 1994].

$$\Delta\tau_c = \Delta\tau_s + \mu_f \Delta\tau_n. \quad (2)$$

In this equation, μ_f is the effective coefficient of friction and $\Delta\tau_n$ and $\Delta\tau_s$ are the normal and shear stresses from the perturbing stress tensor $\Delta\tau_{ij}$ on a plane with normal vector n_i, defined as in *Fialko et al.* [2005] as

$$\Delta\tau_n = \Delta\tau_{ij} n_i n_j \text{ and} \quad (3)$$

$$\Delta\tau_s = \Delta\tau_{ij} n_i t_j, \quad (4)$$

where we use the standard summation notation, such that a variable with a single subscript i or j is a vector, a variable with two subscripts ij is a tensor, and a repeated index indicates summation over the spatial coordinates. Calculating normal stress requires only a choice of the normal to the plane n_i, but calculating shear stress requires choosing both the orientation of the plane and the direction within the plane in which the shear stress is resolved t_i. This will generally be the expected direction of slip on a fault so for the strike-slip SAF, t_i is horizontal along strike, but for the oblique-thrust CSZ, t_i dips in the direction of convergence 69° east of north [*Demets et al.*, 1990; *Demets et al.*, 1994]. A positive or negative change in Coulomb stress indicates that failure along that plane would be promoted or inhibited such that the timing of the subsequent rupture on that fault would be advanced or delayed. Normal stress is positive in extension and negative in compression, whereas the sense of stress indicated by positive and negative shear stress is context dependent. However, we choose the sign such that a positive change in either normal or shear stress always increases Coulomb stress and vice versa. It is worth noting that in regions where normal stress perturbation dominates, the effect on Coulomb stress will be mitigated by the coefficient of friction, but shear stress perturbations have a direct effect on Coulomb stress independent of the coefficient of friction.

[17] The sign and magnitude of the Coulomb stress perturbation on a fault is influenced both by the orientation and presumed sense of slip on that fault and the orientation of the principal stresses of the ocean loading perturbation $\Delta\tau_{ij}$. The intermediate principal stress σ_2 is generally parallel to the coast. Near the shoreline, the maximum (extension) and minimum (compression) principal stresses σ_1 and σ_3 are perpendicular to the coast and plunge roughly 45° away from and toward the ocean, respectively, in the top half of the plate (Figure 2a). Farther onshore, the principal stresses rotate slightly toward the land, whereas farther offshore, they rotate slightly away from the land. Change in normal stress resolved on a vertical onshore fault is extensional because the maximum principal stress is more horizontal (Figure 2b, right). Conversely, normal stress on an offshore fault becomes more compressional (Figure 2b, left). For a vertical strike-slip fault the change in shear stress is much smaller than the change in normal stress. For a shallow dip-slip fault, however, shear stress may be large enough to contribute to Coulomb stress perturbation (Figure 2c). The sense of the change in shear stress will depend on the dip of the fault relative to the orientation of the principal stresses. Shear stress on a coastal fault dipping toward the land is perturbed in a normal shear sense as long as the dip of the fault is shallower than the dip of the compressional principal stress.

3. Results

3.1. Eustatic Ocean Loading at the San Andreas System

[18] The San Andreas fault system accommodates 40 mm/yr of right lateral slip, approximately 80% of the relative Pacific-North American plate motion [e.g., *Demets et al.*, 1990; *Fay and Humphreys*, 2005]. The principal strand of the fault runs within 100 km of the coastline along most of its 500 km length. We calculate the stress change at 10 km depth within a 50 km thick plate in response to 120 m of sea level rise. Figure 4a shows the regional variations in

normal stress resolved on a vertical fault plane striking 50° west of north, the mean trend of the SAF and the various subparallel auxiliary faults that make up the plate boundary. As expected, the regional effect of ocean loading on vertical faults is extension (positive normal stress) onshore and compression (negative normal stress) offshore. These zones of perturbed stress have magnitudes up to 1.5 MPa and follow the coastline, coinciding with the flexural bulge onshore and flexural moat offshore. Stress on a vertical fault running along the shoreline would be perturbed very little by ocean loading. Offshore faults such as those in the borderland of southern California would experience normal compression due to sea level rise. On the basis of the location of the fault trace, the central and southern portions of the SAF would experience more normal extension than the northern SAF and some smaller faults like the Hayward, San Jacinto, and Elsinore faults could experience similar or greater stress perturbations.

[19] The SAF is not, of course, a single plane but rather has significant variation in strike and dip in the central and southern segments (Figure 4c). It dips southwest in the central section, north of the "big bend," and dips northeast south of the "big bend" [*Scheirer et al.*, 2007]. We calculate the normal, shear, and Coulomb stresses resolved on the main SAF strand applying equations (2–4), using the varying orientation and assuming a horizontal in-plane shear direction. Because the strike of the fault roughly follows the shape of the coastline, variations in the dip of the fault have greater influence on stress than variations in strike, decreasing the magnitude of the normal stress (Figure 4b). Along the strike-slip SAF, normal stress is about 4 times larger than shear stress and is the dominant component of Coulomb stress. Assuming an effective coefficient of friction of $\mu_f = 0.6$, Coulomb stress along the SAF is perturbed by 0.5-1 MPa, promoting failure.

[20] A Coulomb stress increase of 1 MPa during the time of eustatic sea level rise corresponds to a loading rate increase of 0.1 kPa/yr, a factor of 300 smaller than the tectonic loading rate of around 30 kPa/yr [*Smith and Sandwell*, 2003]. Over a 300 year seismic cycle, ocean loading would contribute about 30 kPa Coulomb stress. This very small increase in the loading rate on the main fault strand will not noticeably speed up the seismic cycle. However, a change in normal stress of 1 MPa or greater may noticeably weaken (strengthen) the coastal faults onshore (offshore) during times of high sea level relative to times of low sea level. This will be particularly noticeable if fault strength is generally low (10 MPa or less) and remains constant over many seismic cycles. We would expect to see onshore faults have a shorter recurrence interval in recent times than during the LGM, possibly observable on the main strand of the SAF but more likely on the various subparallel secondary faults in the region. Simultaneously, slip on offshore faults would be inhibited, making the recurrence interval longer in recent times relative to the LGM.

3.2. Eustatic Ocean Loading at the Alpine Fault System

[21] Most coastal regions of continents will behave similarly to the San Andreas region when bending in response to a rise in sea level. In areas where loading occurs on either a narrow strip of ocean or around a narrow strip of land of width comparable to half the flexural wavelength, however, the resulting bending stresses may be amplified due to the geometry of the load. One example of this is at the North and South islands of New Zealand, which are approximately 200 km wide. The region is tectonically complicated because the islands mark the transition between the Pacific plate subducted beneath the Australian plate in the north and the Australian plate subducted beneath the Pacific in the south. The 480 km long Alpine fault is the main expression of this plate boundary on the South Island, accommodating 27±5 mm/yr of dextral strike slip and 0–12 mm/yr of fault normal shortening, about 75% of the total Pacific-Australia plate motion predicted by global models [*Norris and Cooper*, 2001].

[22] At the northern South Island, the Alpine fault splays into several subparallel faults in the Marlborough fault system, each accommodating some portion of the slip budget, the largest of which is the Hope fault, carrying 23 mm/yr of strike slip. Additionally as much as 4.1 mm/yr of strike slip may be accommodated on the Porters Pass fault, which runs parallel to the Alpine fault east of the Southern Alps and has produced several large ($M > 7$) earthquakes in the Holocene, though there have been no historic ruptures on this fault [*Howard et al.*, 2005]. The orientation of these faults varies significantly along strike. At the far south, the Alpine fault is mostly a single steeply dipping segment and almost purely strike slip. In central South Island, the Alpine consists of many right-stepping segments, dipping ~50° to the southeast, and has a large convergent component. Farther north, the faults of the Marlborough system are vertical and dextral [*Robinson*, 2004].

[23] Figure 5a shows the regional variations in normal stress in response to 120 m sea level rise using the same model parameters as in the previous section and resolved on a vertical fault plane striking 55° east of north. In general, onshore regions experience an extensional perturbation to normal stress whereas offshore regions experience additional compression, just as in the previous section. The magnitude of the onshore perturbation, however, may be up to 2.4 MPa, which is 60% greater than the normal stress perturbation in the SAF region. This is due to the island being loaded on both sides and being the right width such that the bending effects from each coast overlap and add constructively. Along the trace of the Alpine fault (Figures 5b and 5c), bending stress magnitude varies. In the southern South Island, the Alpine fault runs very near the coastline in the nodal region, such that the perturbation in normal stress on a steeply dipping fault is 1 MPa or less. In the central South Island, the fault has a shallower dip, which tends to decrease the normal stress perturbation, but the fault trace also runs inland, closer to the onshore flexural bulge. The normal stress perturbation in this section is therefore about 1.2 MPa. In the northern Marlborough faults region, change in normal stress is large both because the faults are located in the flexural bulge and because these faults are nearly vertical, such that normal stress is perturbed up to 2 MPa or more in this region.

[24] Assuming a coefficient of friction of $\mu_f = 0.6$ and taking into account the shear stress effects due to changes in the strike of the fault relative to the strike of the coastline, Coulomb stress along the fault is perturbed by 0.5–1.0 MPa. This is similar to the Coulomb stress perturbation at the SAF, so again, we expect that this change will be insignificant compared to the tectonic loading rate. However, because the normal stresses are higher, particularly in the inland sections of the South Island, it is possible that the strength of the Marlborough faults and Porters Pass faults would be

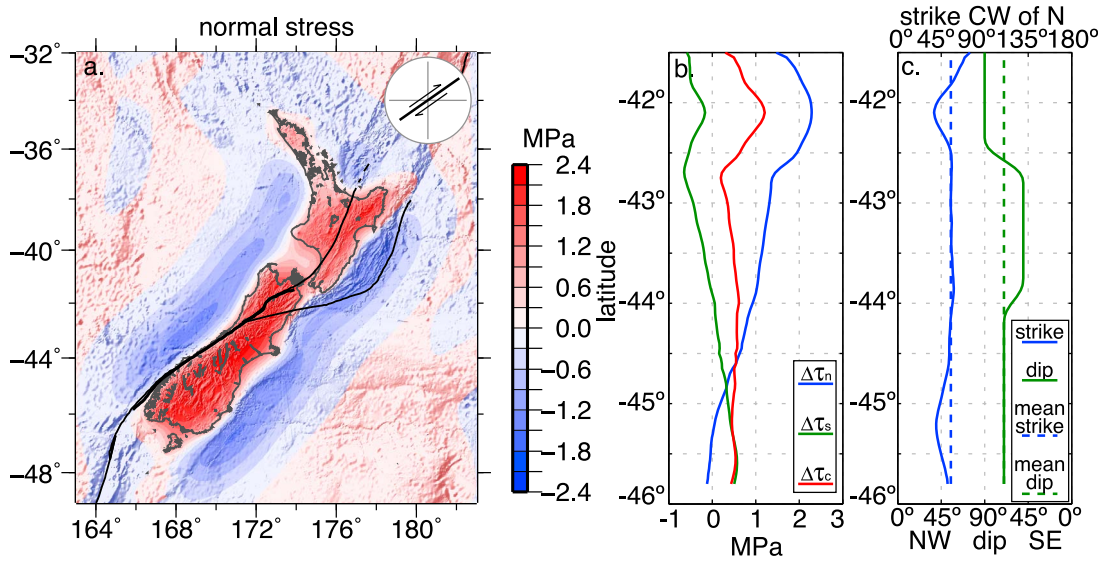

Figure 5. (a) New Zealand region ocean loading perturbation to normal stress resolved on a vertical plane striking 55°E of north. Actual Alpine fault trace shown (thick black line). Positive and negative normal stresses represent extensional and compressional perturbations, respectively. (b) Normal (blue), shear (green), and Coulomb stress (red) resolved onto the Alpine fault plane with varying orientation (c) along its length.

decreased during times of high sea level leading to increased seismic activity and perhaps average slip rate relative to times of low sea level.

3.3. Eustatic Ocean Loading at the Cascadia Subduction System

[25] A third type of coastal plate boundary geometry to consider is the case of a very shallow dipping subduction zone in which the seismogenic zone of the main fault may straddle both sides of the coastline. The Cascadia subduction zone in the Pacific Northwest forms the main boundary between the subducting Juan De Fuca plate and the overriding North America plate. The leading edge of subduction roughly follows the coastline about 100 km offshore, and the base of the locked zone is downdip at a depth around 10 km (Figure 6) [*Fluck et al.*, 1997; *Wang et al.*, 2003]. Using the same parameters as in the previous sections, we calculate the fully relaxed stress change in response to 120 m of sea level

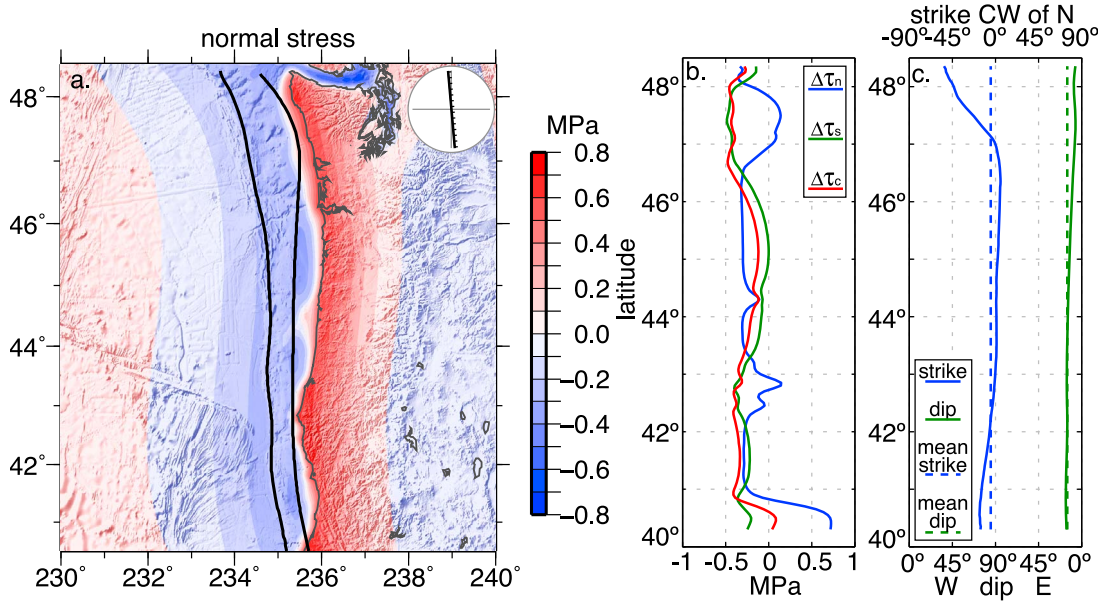

Figure 6. (a) Cascadia region ocean loading perturbation to normal stress resolved on a plane striking 5°W of north and dipping 15°E. CSZ surface trace and approximate location of fault plane at 10 km depth are shown (thick black lines). Positive and negative normal stresses represent extension and compression, respectively. (b) Normal (blue), shear (green), and Coulomb stress (red) resolved onto the actual CSZ plane at 10 km depth with varying orientation (c) along its length.

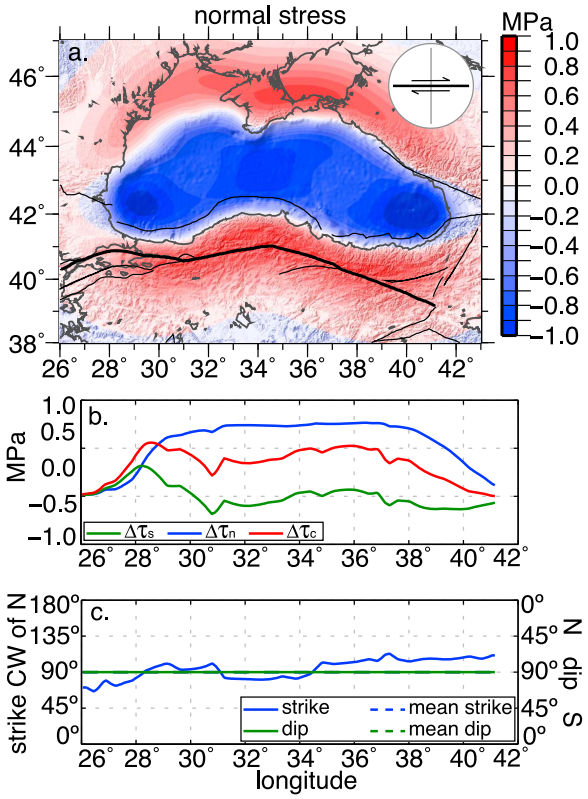

Figure 7. (a) North Anatolian region perturbation to normal stress following inundation of the Black Sea resolved on a vertical plane striking east to west. Actual NAF trace shown (thick black line). Positive and negative normal stresses represent extension and compression, respectively. (b) Normal (blue), shear (green), and Coulomb stress (red) resolved onto the actual NAF plane with varying orientation (c) along its length.

rise and resolve normal stress onto a plane dipping 15° to the east and striking 5° west of north. Normal stress is perturbed by up to 0.6 MPa but in an opposite sense on different parts of the fault. On the shallow offshore portion, failure is inhibited by increased compression, whereas on the downdip extension of the fault beneath the continent failure is promoted by extension on the fault.

[26] The magnitude of normal stress perturbation along the CSZ is about half the magnitude of the perturbation along the SAF to the immediate south, principally because of the shallow dip of the fault. Note, however, that for a similar locking depth the area of a 15° dipping fault will be 3.8 times greater than the area of a vertical fault, so the change in integrated fault strength could be greater at a subduction zone than on a transform fault. The shear stress perturbation along the CSZ is larger than along the SAF, mostly because the sense of shear on the CSZ is thrust motion as opposed to strike slip, and tends to inhibit failure along the coastline. A smaller coefficient of friction in this region, $\mu_f = 0.4$ [*Goldfinger et al.*, 2008], makes the Coulomb stress perturbation at 10 km depth near the shoreline about −0.4 MPa inhibiting failure, smaller than at either the SAF or Alpine fault and corresponding to a stress perturbation rate of −0.04 kPa/yr, much smaller than the tectonic loading rate. Because the fault zone straddles the coastline, the relative strengthening and weakening of different sections of the fault could possibly lead to a shift in the type of rupture on the CSZ. When sea level is high, the CSZ would preferably fail in deeper segments below the continent, whereas in times of low sea level, the CSZ would preferable rupture the shallower offshore portions of the fault zone.

3.4. Rapid Sea Level Rise at the Black Sea

[27] Thus far, we have considered stress perturbations from the steady and gradual increase of eustatic sea level since the LGM. There are, however, cases where water levels, either globally or locally, rose significantly faster than the global post-LGM average. In these instances, the more rapid loading may have had a greater impact on the seismic cycle of nearby faults. In particular, we consider the case of the inundation of the Black Sea, which may have impacted the seismic cycle of the nearby North Anatolian fault.

[28] At the LGM, the connection between the Black Sea and the global ocean was blocked. The subsequent water level of the sea was isolated from eustatic sea level rise until the two reconnected sometime around 10 ka before present. The exact timing and mechanism of reconnection are the subject of ongoing research, but it is generally agreed that shortly before marine reconnection, the level of the Black Sea was significantly low (−100 m). Following reconnection the water level rose ~70 m to the level of the global ocean within a few years to a few hundred years [e.g., *Chepalyga*, 2007; *Hiscott et al.*, 2007; *Major et al.*, 2006; *Ryan*, 2007; *Ryan et al.*, 1997]. Either way, loading at the Black Sea happened at least an order of magnitude faster than in the global ocean. The strike-slip North Anatolian fault (NAF) lies within 100 km of the southern coast of the Black Sea and is well located to be affected by the rapid water level rise (Figure 7a).

[29] When calculating stresses from a more rapidly increasing load, the time evolution of the stress response becomes dependent more on the viscous relaxation rate of the asthenosphere rather than on the loading rate. Initially, we assume a thick elastic plate over a viscoelastic half-space with a shear modulus of $\mu = 28$ GPa and a Maxwell relaxation time $\tau_m = 2\eta/\mu$ of 50 years, corresponding to viscosity $\eta = 2.2 \times 10^{19}$ Pa s. Full relaxation from the sudden Black Sea rise should be complete within 5 Maxwell times, or about 250 years, though eustatic sea level rise would continue to perturb stress at the NAF. Figure 7a shows the fully relaxed regional normal stress from 70 m of inundation calculated on a vertical plane striking east to west at 10 km depth within a 50 km thick elastic plate, and Figure 7b shows the normal, shear, and Coulomb stress perturbations along the NAF assuming a vertical plane with varying strike (Figure 7c). The change in normal stress along the NAF is positive with a maximum magnitude of 0.8 MPa. Along most of the NAF, the shear stress contributions are relatively minor, so the maximum Coulomb stress perturbation is about 0.5 MPa promoting failure, assuming the coefficient of friction $\mu_f = 0.6$. Offshore, the stress perturbations have the opposite sign but an even larger magnitude.

[30] When averaged over the full $5\tau_m$ relaxation time, this suggests an additional Coulomb stress rate of 2 kPa/yr, more than an order of magnitude greater than the eustatic perturbation rate. A viscoelastic material, however, will respond even more rapidly soon after the load is emplaced and will

retard with time. The immediate elastic response to the Black Sea filling increases Coulomb stress along the NAF by about 75 kPa. There is also much uncertainty in the appropriate half-space viscosity for this region. If η were larger, the rapid loading rate would be offset by the slower stress evolution, and the perturbation to Coulomb stress rate on the NAF would more resemble that of eustatic loading on the SAF. However, if η were smaller by a factor of 3, the Maxwell relaxation time would be reduced to about 17 years and the Coulomb stress rate on the NAF would increase by an average 7.2 kPa/yr following inundation. This is about a quarter of the tectonic loading rate. If this were the case, it would certainly impact the seismic cycle, especially immediately after loading, bringing the NAF significantly closer to failure.

[31] It is possible that soon after the Black Sea level rose, all portions of the NAF would have ruptured, regardless of where they had been in their seismic cycle. This could have initiated fault behavior similar to that seen today in which temporally close large earthquakes rupture nearly the entire span of the NAF within about a century [e.g., *Hartleb et al.*, 2006]. Since the time of this water level rise, around 30 seismic cycles have elapsed, so the NAF synchronized rupture we see today is unlikely to be in continued response to the Black Sea increase. But if the paleoseismic record could be extended back to the time of the Black Sea filling, we should be able to clearly observe a marked difference in faulting behavior during the period after Black Sea level rise.

4. Discussion

[32] The ultimate way to test these predictions would be to compare them to a set of paleoseismic data that spanned the last glacial cycle. The paleoseismic observations would need to show either specific ruptures or mean recurrence interval with enough temporal resolution to be able to distinguish between activity at the LGM, activity in the early Holocene, and activity in the late Holocene. If a record was long enough, we would expect to see, e.g., an increase in onshore transform fault activity since the LGM. Unfortunately, complete data sets spanning this interval are largely unavailable. Some paleoseismic records at the SAF or NAF may go back a few thousand years [e.g., *Fumal et al.*, 2002; *Hartleb et al.*, 2006], but these are unable to yield any information about the effect of changing sea level because this is still after the global oceans reached modern levels. In the Dead Sea region, a long paleoseismic record showing some earthquake clustering exists for the late Pleistocene [*Marco et al.*, 1996], but no data sets span the time since the LGM. Recent paleoseismic studies at the Manteigas-Bragança fault in northern Portugal identified a cluster of events 14.5−11 ka [*Rockwell et al.*, 2009]. This sinistral fault lies 120 km inland and has a very low slip rate (<1 mm/yr), and the increase in activity coincides with the most rapid sea level rise. As such, these ruptures may have been promoted by the extra extensional stress provided by bending in response to the seawater load.

[33] Perhaps the most temporally consistent paleoseismic indicators come from some locations, such as at the CSZ, where a marine turbidite record may be used as a proxy for earthquake record [*Goldfinger et al.*, 2003]. Because these rely on offshore sediment cores, they tend to be more complete and extend further back than paleoseismic records from trenching. The record from offshore Cascadia extends 9 ka, and it is tempting to look for an ocean loading signal in these data. In fact, *Goldfinger et al.* [2008; 2003] do calculate a different recurrence interval for the northern SAF and CSZ over the last 3ka ($\tau_r \sim 215$ years) versus the last 9ka ($\tau_r \sim 260$ year). If these differences were real, they would suggest that the seismic cycle at the northern SAF and CSZ sped up slightly as sea level rose, which would be consistent with our prediction that flexure in response to sea level rise promotes failure onshore. However, these observations are not robust and the authors themselves caution against drawing any conclusions about long-term fault behavior from this data set. Future paleoseismic studies may be able to either extend existing records to the late Pleistocene, or further establish records on very low-slip faults, thus providing a record that could better test for the influence of sea level rise on plate boundary behavior. For the time being, however, the question of "was ocean loading important" remains unclear.

[34] Instead, we focus on the question "could ocean loading have been important"? There are two ways to interpret the calculated change in Coulomb stress. If faults are weak, i.e., they consistently slip when accumulated shear stress reaches a low threshold value (~10 MPa) [e.g., *Zoback et al.*, 1987], then either increasing or decreasing the normal stress on the fault by a megapascal or more through the process of ocean loading could be an important change that modulates fault behavior. As sea level rises and falls in response to the Milankovitch cycles, the normal stress on coastal faults will also vary cyclically, promoting onshore fault failure when ocean levels are high, inhibiting onshore fault failure when ocean levels are low and vice versa for offshore faults. Indeed, if a record of plate boundary activity spanning the Pleistocene were available, we would expect cyclically enhanced and muted failure of coastal faults following the oscillating ocean loading. If, however, faults are very strong or fault strength has little consistency beyond a few seismic cycles, variations in stress accumulation rate may be more important, in which case the few pascals per year difference will probably not noticeably alter the seismic cycle at plate boundary faults.

[35] In either case, because the ocean loading perturbation to normal stress is relatively uniform across the flexural bulge, we expect all the faults in a plate boundary region to experience roughly the same bending stress from ocean loading. Any perturbation to the seismic cycle would be more evident on a secondary fault structure with a low tectonic loading rate than on the principal strand of the plate boundary. Thus, in the San Andreas region, for example, we expect ocean loading to noticeably promote failure on the faults of the eastern California shear zone or the Los Angeles basin but to inhibit failure on the Garlock fault due to its orientation and sense of slip. It is also possible that coastal faults at passive continental margins could be influenced, or even reactivated, by ocean loading.

[36] We can extend the analysis of the SAF, Alpine fault, and CSZ presented here to infer the effect of sea level rise in other regions. In general, we expect seismic activity to increase onshore and decrease offshore. Particularly, we expect muted activity in regions where the ocean load is narrow, such as in the fledgling rift zones or other narrow gulfs, and enhanced activity in regions where the ocean load surrounds a narrow strip of land, such as at the Italian

peninsula, the islands of Japan, or the isthmus of Central America. This amplification of the ocean loading effect depends upon the features having a width comparable to half the flexural wavelength of the bending plate and will therefore vary from region to region. At coastal subduction zones, we might anticipate a cyclic shift between deep and shallow activity following the variations in sea level. This effect ought to be particularly noticeable on the islands of Japan, which both override a subducting plate and are loaded by changes in sea level on multiple sides.

[37] The model calculations presented in this study are dependent upon the choice of some physical parameters. A thicker plate would result in more widespread stresses of smaller magnitude and vice versa. A more or less viscous half-space has ramifications for the temporal importance of the loading rate relative to the relaxation rate, as discussed in the previous section. We have assumed a half-space viscosity corresponds to a single relaxation time, regardless of the wavelength of the load. Such an assumption may be a simplification of the true physics involved in viscous relaxation, but it is appropriate in this case because the load primarily consists of a single wavelength, that of the flexural wavelength of the plate. We have also assumed the thick plate is a perfect elastic solid, corresponding to a Poisson's ratio of 0.25, but this number may be higher. We compared the model output for a Poisson's ratio of $\nu = 0.25$ and $\nu = 0.5$, corresponding to an incompressible elastic solid, and found that increasing the Poisson's ratio increases the magnitude of all the stresses by about 20%. Since the stress patterns produced also do not change, the overall effect of a variation in Poisson's ratio is small and would not alter the interpretation of the modeled stresses. The model presented here is particularly well suited for calculating stresses from relatively small, short wavelength loads, such that a flat earth approximation is valid and the physical processes involved can be acceptably characterized as linear. As such, it would be inadequate for investigation of broader loads such as postglacial rebound in the polar regions, where additional physics would be required.

[38] There have also been certain simplifications of loading processes in that while focusing on the loading of water mass accumulated in the oceans, we have neglected any mass unloading caused by ice melting that happens over the same time period. While the large scale continental ice sheets may be far enough removed from most active plate boundaries to affect the ocean loading process, there may have been considerable ice mass stored in mountain glaciers that existed in proximity to coastal plate boundaries. Had we included this additional source of onshore unloading, offshore compression and onshore extension would still be predicted for coastal regions, only the magnitude of onshore extension would increase by an amount related to the size and proximity of the glacier. In such a case, activity at onshore faults would be even greater at sea level highstands relative to the times of glacial maximum and an observable signal would be even more likely.

[39] Another implication of this study is a reemphasis that a seismic cycle can be modulated by factors external to it. The consistent discrepancies in fault slip estimates from geologic and geodetic methods may be reconcilable as the various estimation methods evolve and improve. However, persistent discrepancies may reveal actual temporal variation in instantaneous slip rate [*Bennett*, 2007] and thus subtle details of the long-term faulting process, including the transfer of plate boundary slip between different active fault strands. Stress perturbations from sea level rise and their effect on seismic cycles could be significant enough that a geologic estimate of slip rate estimated over this time period would be expected to differ from a modern geodetic slip rate. At onshore transform boundaries such as the SAF, Alpine Fault, or NAF, we would generally expect $v_{\mathrm{geologic}} < v_{\mathrm{geodetic}}$. Again, this ocean loading-induced slip rate discrepancy would be more pronounced on low-slip secondary faults than on principal plate boundary strands. When trying to understand long-term fault system behavior, we find it may be at least as important to consider stresses external to the system as to consider subtle seismic cycle stresses internal to the system. Particularly, we reemphasize the ability of climate systems to interact with tectonic systems.

5. Conclusions

[40] We have investigated the theoretical role of eustatic sea level changes in modulating the seismic cycle at coastal plate boundary systems. Sea level rise induces bending about coastlines globally, reducing the magnitude of normal stress so as to "unclamp" onshore faults and promote failure while altering normal stress on offshore faults so as to inhibit failure. A near shore transform fault will experience a 1−2 MPa change in normal stress over this time period, promoting failure onshore and inhibiting it offshore, corresponding to a change in Coulomb stress accumulation rate of ~100 Pa/yr. This rate is about 100 times smaller that the tectonic loading rate on major plate boundaries and will therefore not alter the stress buildup on a fault. However, the total magnitude of normal stress change may perceptibly weaken or strengthen coastal faults, particularly if the background fault strength is low and remains constant over many seismic cycles, thus altering the quantity of tectonically accumulated stress required for the fault to rupture.

[41] For coastal transform faults, those onshore will be weaker during periods of high sea level (such as today) relative to periods of low sea level (such as during the LGM), corresponding to a more rapid seismic cycle. Offshore transform faults will be relatively stronger when sea level is high, with less activity relative to times of low sea level. It is possible that these nontectonic influences on the seismic cycle could be detected at major plate boundary faults such as the SAF or AFNZ. However, it is more likely that the influence of plate bending in response to ocean loading would be observable on secondary faults with a much lower tectonic loading rate. In locations where sea level rise was much faster than the global average, such as in the catastrophic flooding of the Black Sea, the same normal stress perturbation of up to 1 MPa develops over a much shorter period of time, determined by the relaxation time of the asthenosphere. Following this event, the Coulomb stress accumulation rate on the onshore North Anatolian Fault increased by as much as 2 kPa/yr for a few hundred years. This rapid decrease in fault strength would likely have encouraged all segments of the NAF to rupture soon after the load was emplaced, though it is unlikely that this pattern of rupture would persist over tens

of seismic cycles to be related to the synchronicity of NAF ruptures observed today.

Appendix A

[42] We calculate the full 3-D stress tensor from a vertical surface load on a thick elastic plate overlying a Maxwell viscoelastic half-space. The model is semianalytic in that we convolve the response of a unit point load on a thick elastic plate overlying a viscoelastic half-space with the true load distribution in the Fourier domain. It is this delta function response that we now further derive.

[43] The 3-D problem is solved analytically in the vertical and time dimensions (z, t), whereas the solutions in the horizontal dimensions (x, y) are developed in the Fourier transform domain. This semianalytic method allows us to take full advantage of the convolution theorem and the numerical efficiency of the fast Fourier transform, while maintaining an arbitrarily complex surface load distribution. The disadvantage is that the rheology is restricted to stacked homogeneous layers.

[44] The original solution of the Boussinesq problem [*Boussinesq*, 1885] was for vertical tractions on a homogeneous elastic half-space. *Steketee* [1958] used this solution to balance the anomalous vertical tractions resulting from a force couple model. *Smith and Sandwell* [2004] followed these methods to develop a solution for vertical tractions on an elastic plate over a viscoelastic half-space, again using the solution to correct anomalous vertical tractions resulting from a force couple model. *Luttrell et al.* [2007] adapted this Boussinesq-like vertical traction calculation to calculate displacement and stress in the lithosphere near the southern San Andreas fault in response to the time varying load of Ancient Lake Cahuilla.

[45] We develop the solution in two parts (for further details of development and testing, see *Smith and Sandwell* [2004]). First, we derive the solution for displacement and stress in a layered elastic half-space (homogeneous layer with Lamé parameters μ_1 and λ_1 over a homogeneous elastic half-space with Lamé parameters μ_2 and λ_2). Second, we use the correspondence principle to simulate viscoelastic behavior in the lower half-space by allowing the effective shear modulus μ_2 to vary with the time elapsed since loading t relative to the Maxwell time of the half-space τ_{m}.

A1. Normal Traction on a Layered Elastic Half-space

[46] Following the method of *Steketee* [1958], we let displacement and stress be a function of the Galerkin vector potential Γ_i,

$$u_i = \Gamma_{i,kk} - \alpha\Gamma_{k,ki}, \tag{A1}$$

$$\tau_{ij} = \lambda(1-\alpha)\delta_{ij}\Gamma_{l,kkl} + \mu\left(\Gamma_{i,kkj} + \Gamma_{j,kki}\right) - 2\mu\alpha\Gamma_{k,kij}, \tag{A2}$$

where α is a constant yet to be determined and stress τ_{ij} has been related to strain and displacement u_i through an elastic constitutive equation with Lamé parameters λ and μ. Note that we use the standard summation notation, such that a variable with a single subscript is a vector, a variable with two subscripts is a tensor, a repeated index indicates summation over the spatial coordinates, and an index following a comma indicates differentiation with respect to that spatial coordinate. Because our point source is a purely normal traction on the free surface of a layered half-space, it turns out that we need only retain the third component of the Galerkin vector, such that $\Gamma_x = \Gamma_y = 0$ and $\Gamma_z = \Gamma$, which we shall now call the Galerkin potential.

[47] The equilibrium equations for a body in the absence of internal body forces or acceleration are $\tau_{ij,j} = 0$. When we write these as a funtion of Galerkin potential, we find that with a clever choice of $\alpha = (\lambda + \mu)/(\lambda + 2\mu)$, the Galerkin potential must satisfy the biharmonic equation $\nabla^4\Gamma = 0$. After taking the 2-D horizontal Fourier transform of this equation, the solution form is recognized as

$$\Gamma(\mathbf{k}, z) = (A + Cz)e^{2\pi|\mathbf{k}|z} - (B + Dz)e^{-2\pi|\mathbf{k}|z}, \tag{A3}$$

where $|\mathbf{k}| = \sqrt{k_x^2 + k_y^2}$ is the horizontal wave number and (A, B, C, D) are coefficients to be determined by the boundary conditions. Our layered model consists of an elastic layer of thickness h (z positive up) over an elastic half-space, and the solution will require a Galerkin potential for each layer related to stress and displacement by the elastic moduli of that layer (Γ_1, μ_1, λ_1, α_1 in the upper layer, Γ_2, μ_2, λ_2, α_2 in the lower half-space).

[48] There are three boundary conditions that must be met for our layered elastic half-space: (1) a normal traction τ_{applied} is applied at the free surface and is partially balanced by a gravitational restoring force, but shear tractions must be zero

$$\begin{aligned} \tau_{zz1}\big|_{z=0} &= -\tau_{\mathrm{applied}} + \rho_1 g W_1\big|_{z=0} \\ \tau_{xz1}\big|_{z=0} &= \tau_{yz1}\big|_{z=0} = 0 \end{aligned}; \tag{A4}$$

(2) all components of displacement and stress must be continuous across the boundary between the layer and the half-space (note that we have shifted notation for displacement such that $u_x = U$, $u_y = V$, and $u_z = W$)

$$\begin{aligned} U_1\big|_{z=-h} &= U_2\big|_{z=-h} \quad \tau_{xz1}\big|_{z=-h} = \tau_{xz2}\big|_{z=-h} \\ V_1\big|_{z=-h} &= V_2\big|_{z=-h} \quad \tau_{yz1}\big|_{z=-h} = \tau_{yz2}\big|_{z=-h} \\ W_1\big|_{z=-h} &= W_2\big|_{z=-h} \quad \tau_{zz1}\big|_{z=-h} = \tau_{zz2}\big|_{z=-h} \end{aligned}; \tag{A5}$$

(3) at infinite depth, all stress and displacement components must go to zero.

$$\begin{aligned} \tau_{xz2}\big|_{z\to\infty} &= \tau_{yz2}\big|_{z\to\infty} = \tau_{zz2}\big|_{z\to\infty} = 0 \\ U_2\big|_{z\to\infty} &= V_2\big|_{z\to\infty} = W_2\big|_{z\to\infty} = 0. \end{aligned} \tag{A6}$$

[49] The boundary conditions (A4–A6) can be rewritten in terms of the Galerkin potential (A1–A3) resulting in a set of equations with eight coefficients, (A_1, B_1, C_1, D_1) and (A_2, B_2, C_2, D_2). The third boundary condition is solved by ensuring $B_2 = D_2 = 0$, so we are left finally with six coefficients (A_1, B_1, C_1, D_1, A_2, C_2) and six equations

$$\begin{aligned} & & U_1\big|_{z=-h} &= U_2\big|_{z=-h} \\ \tau_{xz1}\big|_{z=0} &= 0 & W_1\big|_{z=-h} &= W_2\big|_{z=-h} \\ \tau_{zz1}\big|_{z=0} &= -\tau_{\mathrm{applied}} + \rho_1 g W_1\big|_{z=0} & \tau_{xz1}\big|_{z=-h} &= \tau_{xz2}\big|_{z=-h} \\ & & \tau_{zz1}\big|_{z=-h} &= \tau_{zz2}\big|_{z=-h} \end{aligned}. \tag{A7}$$

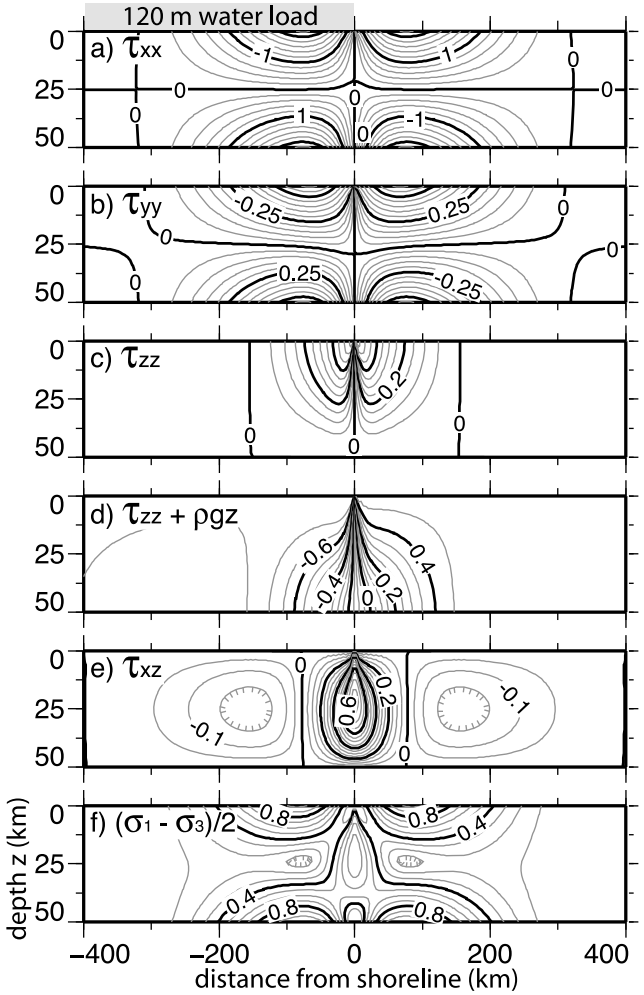

Figure A1. Contours of stress components, in units of MPa, as a function of depth and distance perpendicular to a coastline that has been loaded on one side by 120 m of water and allowed to fully relax. Horizontal normal components of bending stress (a) perpendicular to shoreline and (b) parallel to shoreline. (c) Vertical normal component of bending stress. (d) Vertical normal component of bending stress plus stress from a buoyant mantle deflection. (e) Vertical shear stress component perpendicular to the shoreline (note the other two shear stress components τ_{xy} and τ_{yz} are negligible for a straight coastline oriented along the y axis). (f) Maximum shear stress induced by bending stresses across the coastline.

(Note that there is some redundancy in the algebra because we are describing a solution with cylindrical symmetry in a Cartesian coordinate system). We algebraically solve this system of equations using the computer algebra capabilities of MATLAB (see *Smith and Sandwell* [2004, Appendix A] for the solutions to the coefficients (A_1, B_1, C_1, D_1, A_2, C_2)). MATLAB also delivers C-code for the rather complicated algebraic forms that can be directly used in computation, although the code does need to be modified to ensure that there are no growing exponential functions to cause numerical problems. We can then use equations (A1–A3) to calculate stress and displacement as a function of k_x, k_y, z, and $\tau_{\text{applied}}(k_x, k_y)$, the Fourier transform of the applied load, and inverse Fourier transform to get numerical solutions for the stress and displacement components in the space domain.

[50] Because the horizontal dimensions are solved in the Fourier domain, the horizontal boundary conditions require that stress and strain be periodic. We deal with this by tapering the edges of our flat earth grids to zero, thus ensuring periodicity in all directions. This means that we are restricted to examining features of interest of characteristic wavelength smaller than the length of the grid. For a typical regional grid of 2048 × 2048 elements at a grid spacing of 30 arc sec (~1 km), this means we are limited to features with characteristic wavelength less than ~1000 km. This resolution is sufficient since we are focused on the coastline transitions along a specific segment of a plate boundary.

A2. Including Time Dependence With a Maxwell Viscoelastic Model

[51] A viscoelastic Maxwell body is made up of an elastic element and a viscous element connected in series. Its constitutive equation is

$$\dot{\varepsilon} = \frac{1}{\mu}\dot{\sigma} + \frac{1}{\eta}\sigma, \tag{A8}$$

where σ and ε are stress and strain, respectively; μ and η are the shear modulus and viscosity, respectively, and the over dot indicates the time derivative. Making use of the correspondence principle, we take the Laplace transform of (A8) (where s is the Laplace domain variable) and solve for stress

$$\sigma(s) = \frac{\mu s}{s + \frac{\mu}{\eta}}\varepsilon(s). \tag{A9}$$

If we let the effective shear modulus be

$$\mu_2(s) = \frac{\mu s}{s + \frac{\mu}{\eta}}, \tag{A10}$$

we can then write

$$\sigma(s) = \mu_2(s)\varepsilon(s), \tag{A11}$$

which is in the same form as an elastic constitutive relation. Note that when we solve for an effective lower shear modulus μ_2, we must also solve for an effective Lamé parameter λ_2 so that the bulk modulus of the half-space remains constant.

[52] We can analytically inverse Laplace transform (A10) and get

$$\mu_2(t) = \mu\left(\frac{e^{-\frac{t}{\tau_m}}}{2 - e^{-\frac{t}{\tau_m}}}\right), \tag{A12}$$

where we have assumed a single Maxwell relaxation time τ_m for the material regardless of the wavelength of the load, defined by

$$\tau_m = \frac{2\eta}{\mu}. \tag{A13}$$

So given a time since loading and a Maxwell relaxation time, we can compute the effective Lamé parameters of the lower half-space and then use those in the layered elastic solutions for stress and displacement.

A3. Model Benchmarks

[53] The end-member cases of this model have been benchmarked against known solutions. The elastic half-space end-member should match the analytic displacement solutions of *Love* [1929], and the elastic plate over a fluid end member should approximate the numerical displacement and stress solutions for flexure of a thin elastic plate [*Turcotte and Schubert*, 2002]. The model has been found to be in good agreement with both sets of solutions [*Luttrell et al.*, 2007; *Smith and Sandwell*, 2004]. Additionally, we present here contours of the fully relaxed stress components as a function of depth and distance perpendicular to a straight coastline, parallel to the y axis, which has been loaded on one side ($x < 0$) by 120 m of water (Figure A1). All three components of normal stress are in compression underneath the load and in extension "onshore" in the top half of the plate, with stronger magnitudes near the surface, away from the nodal plane. The component of vertical shear stress perpendicular to the coastline is maximized in a narrow zone at the coastline and is stronger in the middle of the plate than at the surface. The maximum shear stress $(\sigma_1 - \sigma_3)/2$, where σ_1 and σ_3 are the maximum and minimum principal stresses, reflects the patterns of the other stress components with high magnitudes near the surface offshore and onshore and high magnitudes at depth at the coastline. When computed for an elliptical disc-shaped load of the same dimensions, these stress components match those published in studies by *Ivins et al.* [2003], *Klemann and Wolf* [1998], and *Johnston et al.* [1998], though we note the vertical normal stress τ_{zz} of those models corresponds to the vertical normal stress of our bending model with an additional stress due to the buoyancy of the deflected mantle, $\tau_{zz} + \rho_m g W$.

[54] **Acknowledgments.** We thank B. Bills, T. Rockwell, B. Smith-Konter, and B. Meade for their helpful conversations and feedback in the development of this manuscript. Thoughtful reviews by E. Ivins, K. Heki, and an Associate Editor greatly improved the manuscript. This research was supported by the NASA Earth and Space Science Fellowship Program and by the National Science Foundation (EAR 0811772).

References

Becker, J. J., et al. (2009), Global bathymetry and elevation data at 30 arc seconds resolution: SRTM30_PLUS, *Mar. Geod.*, *32*(4), 355–371, doi:10.1080/01490410903297766.

Bennett, R. A. (2007), Instantaneous slip rates from geology and geodesy, *Geophys. J. Int.*, *169*(1), 19–28, doi:10.1111/j.1365-246X.2007.03331.x.

Bennett, R. A., A. M. Friedrich, and K. P. Furlong (2004), Codependent histories of the San Andreas and San Jacinto fault zones from inversion of fault displacement rates, *Geology*, *32*(11), 961–964, doi:10.1130/G20806.1.

Bettinelli, P., J. P. Avouac, M. Flouzat, L. Bollinger, G. Ramillien, S. Rajaure, and S. Sapkota (2008), Seasonal variations of seismicity and geodetic strain in the Himalaya induced by surface hydrology, *Earth Planet. Sci. Lett.*, *266*(3–4), 332–344, doi:10.1016/j.epsl.2007.11.021.

Bollinger, L., F. Perrier, J. P. Avouac, S. Sapkota, U. Gautam, and D. R. Tiwari (2007), Seasonal modulation of seismicity in the Himalaya of Nepal, *Geophys. Res. Lett.*, *34*, L08304, doi:10.1029/2006GL029192.

Boussinesq, J. (1885), *Application des Potentiels a l'Etude de l'Equilibre et du Mouvement des Solides Elastiques*, 508 pp., Gauthier-Viallars, Paris.

Chepalyga, A. (2007), The late glacial great flood in the Ponto-Caspian Basin, in *The Black Sea Flood Question: Changes in Coastline, Climate, and Human Settlement*, edited by V. Yanko-Hombach, A. Gilbert, N. Panin, and P. Dolukhanov, pp. 63–88, Springer, Dordrecht, The Netherlands.

Chery, J., and P. Vernant (2006), Lithospheric elasticity promotes episodic fault activity, *Earth Planet. Sci. Lett.*, *243*(1–2), 211–217, doi:10.1016/j.epsl.2005.12.014.

Demets, C., R. G. Gordon, D. F. Argus, and S. Stein (1990), Current plate motions, *Geophys. J. Int.*, *101*(2), 425–478.

Demets, C., R. G. Gordon, D. F. Argus, and S. Stein (1994), Effect of recent revisions to the geomagnetic reversal time-scale on estimates of current plate motions, *Geophys. Res. Lett.*, *21*(20), 2191–2194, doi:10.1029/94GL02118.

Dolan, J. F., D. D. Bowman, and C. G. Sammis (2007), Long-range and long-term fault interactions in Southern California, *Geology*, *35*(9), 855–858, doi:10.1130/G23789A.1.

Fay, N. P., and E. D. Humphreys (2005), Fault slip rates, effects of elastic heterogeneity on geodetic data, and the strength of the lower crust in the Salton Trough region, southern California, *J. Geophys. Res.*, *110*, B09401, doi:10.1029/2004JB003548.

Fialko, Y., L. Rivera, and H. Kanamori (2005), Estimate of differential stress in the upper crust from variations in topography and strike along the San Andreas fault, *Geophys. J. Int.*, *160*(2), 527–532, doi:10.1111/j.1365-246X.2004.02511.x.

Fluck, P., R. D. Hyndman, and K. Wang (1997), Three-dimensional dislocation model for great earthquakes of the Cascadia subduction zone, *J. Geophys. Res.*, *102*(B9), 20,539–20,550, doi:10.1029/97JB01642.

Fumal, T. E., M. J. Rymer, and G. G. Seitz (2002), Timing of large earthquakes since AD 800 on the Mission Creek strand of the San Andreas fault zone at Thousand Palms Oasis, near Palm Springs, California, *Bull. Seismol. Soc Am.*, *92*(7), 2841–2860.

Gahalaut, K., V. K. Gahalaut, and M. R. Pandey (2007), A new case of reservoir triggered seismicity: Govind Ballav Pant reservoir (Rihand dam), central India, *Tectonophysics*, *439*(1–4), 171–178, doi:10.1016/j.tecto.2007.04.003.

Goldfinger, C., C. H. Nelson, and J. E. Johnson (2003), Holocene earthquake records from the Cascadia subduction zone and northern San Andreas fault based on precise dating of offshore turbidites, *Annu. Rev. Earth Planet. Sci.*, *31*, 555–577, doi:10.1146/annurev.earth.31.100901.141246.

Goldfinger, C., et al. (2008), Late Holocene rupture of the northern San Andreas fault and possible stress linkage to the Cascadia subduction zone, *Bull. Seismol. Soc. Am.*, *98*(2), 861–889, doi:10.1785/0120060411.

Grollimund, B., and M. D. Zoback (2000), Post glacial lithospheric flexure and induced stresses and pore pressure changes in the northern North Sea, *Tectonophysics*, *327*(1–2), 61–81.

Hampel, A., and R. Hetzel (2006), Response of normal faults to glacial-interglacial fluctuations of ice and water masses on Earth's surface, *J. Geophys. Res.*, *111*, B06406, doi:10.1029/2005JB004124.

Hartleb, R. D., J. F. Dolan, O. Kozaci, H. S. Akyuz, and G. G. Seitz (2006), A 2500 yr long paleoseismologic record of large, infrequent earthquakes on the North Anatolian fault at Cukurcimen, Turkey, *Geol. Soc. Am. Bull.*, *118*(7–8), 823–840, doi:10.1130/B25838.1.

Heki, K. (2001), Seasonal modulation of interseismic strain buildup in northeastern Japan driven by snow loads, *Science*, *293*(5527), 89–92.

Heki, K. (2003), Snow load and seasonal variation of earthquake occurrence in Japan, *Earth Planet. Sci. Lett.*, *207*(1–4), 159–164, doi:10.1016/S0012-821X(02)01148-2.

Hetland, E. A., and B. H. Hager (2006), Interseismic strain accumulation: Spin-up, cycle invariance, and irregular rupture sequences, *Geochem. Geophys. Geosyst.*, *7*, Q05004, doi:10.1029/2005GC001087.

Hetzel, R., and A. Hampel (2005), Slip rate variations on normal faults during glacial-interglacial changes in surface loads, *Nature*, *435*(7038), 81–84, doi:10.1038/nature03562.

Hiscott, R., A. Aksu, P. Mudie, M. Kaminski, T. Abrajano, D. Yasar, and A. Rochon (2007), The Maramara Sea Gateway since ~16 ky BP: Non-catastrophic causes of paleoceanographic events in the Black Sea at 8.4 and 7.15 ky BP, in *The Black Sea Flood Question: Changes in Coastline, Climate, and Human Settlement*, edited by V. Yanko-Hombach, et al., pp. 63–88, Springer, Dordrecht, The Netherlands.

Howard, M., A. Nicol, J. Campbell, and J. R. Pettinga (2005), Holocene paleoearthquakes on the strike-slip Porters Pass Fault, Canterbury, New Zealand, *N. Z. J. Geol. Geophys.*, *48*(1), 59–74.

Ivins, E. R., T. S. James, and V. Klemann (2003), Glacial isostatic stress shadowing by the Antarctic ice sheet, *J. Geophys. Res.*, *108*(B12), 2560, doi:10.1029/2002JB002182.

Ivins, E. R., R. K. Dokka, and R. G. Blom (2007), Post-glacial sediment load and subsidence in coastal Louisiana, *Geophys. Res. Lett.*, *34*, L16303, doi:10.1029/2007GL030003.

James, T. S., J. J. Clague, K. L. Wang, and I. Hutchinson (2000), Postglacial rebound at the northern Cascadia subduction zone, *Quat. Sci. Rev.*, *19*(14–15), 1527–1541.

Johnston, P., P. Wu, and K. Lambeck (1998), Dependence of horizontal stress magnitude on load dimension in glacial rebound models, *Geophys. J. Int.*, *132*(1), 41–60.

Kendall, R., J. X. Mitrovica, and R. Sabadini (2003), Lithospheric thickness inferred from Australian post-glacial sea-level change: The influence of a ductile crustal zone, *Geophys. Res. Lett.*, *30*(9), 1461, doi:10.1029/2003GL017022.

King, G. C. P., and M. Cocco (2001), Fault interaction by elastic stress changes: New clues from earthquake sequences, in *Advances in Geophysics*, vol. 44, pp. 1–38.

King, G. C. P., R. S. Stein, and J. Lin (1994), Static stress changes and the triggering of earthquakes, *Bull. Seismol. Soc Am.*, *84*(3), 935–953.

Klemann, V., and D. Wolf (1998), Modelling of stresses in the Fennoscandian lithosphere induced by Pleistocene glaciations, *Tectonophysics*, *294*(3–4), 291–303.

Lambeck, K., and A. Purcell (2005), Sea-level change in the Mediterranean Sea since the LGM: model predictions for tectonically stable areas, *Quat. Sci. Rev.*, *24*(18–19), 1969–1988, doi:10.1016/j.quascirev.2004.06.025.

Lambeck, K., and J. Chappell (2001), Sea level change through the last glacial cycle, *Science*, *292*(5517), 679–686.

Lambeck, K., T. M. Esat, and E. K. Potter (2002a), Links between climate and sea levels for the past three million years, *Nature*, *419*(6903), 199–206, doi:10.1038/nature01089.

Lambeck, K., Y. Yokoyama, and T. Purcell (2002b), Into and out of the Last Glacial Maximum: Sea level change during Oxygen Isotope Stages 3 and 2, *Quat. Sci. Rev.*, *21*(1–3), 343–360.

Love, A. E. H. (1929), The stress produced in a semi-infinite solid by pressure on part of the boundary, *Proc. R.. Soc. London, Ser. A, 228*, 377–420.

Luttrell, K., D. Sandwell, B. Smith-Konter, B. Bills, and Y. Bock (2007), Modulation of the earthquake cycle at the southern San Andreas fault by lake loading, *J. Geophys. Res.*, *112*, B08411, doi:10.1029/2006JB004752.

Major, C. O., S. L. Goldstein, W. B. F. Ryan, G. Lericolais, A. M. Piotrowski, and I. Hajdas (2006), The co-evolution of Black Sea level and composition through the last deglaciation and its paleoclimatic significance, *Quat. Sci. Rev.*, *25*(17–18), 2031–2047, doi:10.1016/j.quascirev.2006.01.032.

Marco, S., M. Stein, A. Agnon, and H. Ron (1996), Long-term earthquake clustering: A 50,000-year paleoseismic record in the Dead Sea Graben, *J. Geophys. Res.*, *101*(B3), 6179–6191.

Matmon, A., D. P. Schwartz, R. Finkel, S. Clemmens, and T. Hanks (2005), Dating offset fans along the Mojave section of the San Andreas fault using cosmogenic Al-26 and Be-10, *Geol. Soc. Am. Bull.*, *117*(5–6), 795–807, doi:10.1130/B25590.1.

Norris, R. J., and A. F. Cooper (2001), Late Quaternary slip rates and slip partitioning on the Alpine Fault, New Zealand, *J. Struct. Geol.*, *23*(2–3), 507–520.

Oskin, M., L. Perg, D. Blumentritt, S. Mukhopadhyay, and A. Iriondo (2007), Slip rate of the Calico fault: Implications for geologic versus geodetic rate discrepancy in the Eastern California Shear Zone, *J. Geophys. Res.*, *112*, B03402, doi:10.1029/2006JB004451.

Peltier, W. R. (2004), Global glacial isostasy and the surface of the ice-age earth: The ice-5G (VM2) model and grace, *Annu. Rev. Earth Planet. Sci.*, *32*, 111–149, doi:10.1146/annurev.earth.32.082503.144359.

Peltier, W. R., and R. Drummond (2008), Rheological stratification of the lithosphere: A direct inference based upon the geodetically observed pattern of the glacial isostatic adjustment of the North American continent, *Geophys. Res. Lett.*, *35*, L16314, doi:10.1029/2008GL034586.

Peltier, W. R., and R. G. Fairbanks (2006), Global glacial ice volume and Last Glacial Maximum duration from an extended Barbados sea level record, *Quat. Sci. Rev.*, *25*(23–24), 3322–3337, doi:10.1016/j.quascirev.2006.04.010.

Robinson, R. (2004), Potential earthquake triggering in a complex fault network: The northern South Island, New Zealand, *Geophys. J. Int.*, *159*(2), 734–748, doi:10.1111/j.1365-246X.2004.02446.x.

Rockwell, T., J. Fonseca, C. Madden, T. Dawson, L. A. Owen, S. Vilanova, and P. Figueiredo (2009), Paleoseismology of the Vilariça Segment of the Manteigas-Bragança Fault in Northeastern Portugal, in *Palaeoseismology: Historical and Prehistorical Records of Earthquake Ground Effects for Seismic Hazard Assessment*, edited by K. Reicherter, A. M. Michetti, and P. G. Silva, pp. 237–258, doi:10.1144/SP316.15, Geol. Soc. London, London.

Ryan, W. B. F. (2007), Status of the Black Sea flood hypothesis, in *The Black Sea Flood Question: Changes in Coastline, Climate, and Human Settlement*, edited by V. Yanko-Hombach, et al., pp. 63–88, Springer, Dordrecht, The Netherlands.

Ryan, W. B. F., W. C. Pitman, C. O. Major, K. Shimkus, V. Moskalenko, G. A. Jones, P. Dimitrov, N. Gorur, M. Sakinc, and H. Yuce (1997), An abrupt drowning of the Black Sea shelf, *Mar. Geol.*, *138*(1–2), 119–126.

Scheirer, D., G. Fuis, and V. Langenheim (2007), Constructing a Model of a Dipping Southern San Andreas Fault, Southern California, *Eos Trans. AGU*, *88*(52), Fall Meet. Suppl., Abstract H34B-01.

Simpson, D. W., W. S. Leith, and C. H. Scholz (1988), Two types of reservoir-induced seismicity, *Bull. Seismol. Soc Am.*, *78*(6), 2025–2040.

Smith, B., and D. Sandwell (2003), Coulomb stress accumulation along the San Andreas fault system, *J. Geophys. Res.*, *108*(B6), 2296, doi:10.1029/2002JB002136.

Smith, B., and D. Sandwell (2004), A three-dimensional semianalytic viscoelastic model for time-dependent analyses of the earthquake cycle, *J. Geophys. Res.*, *109*, B12401, doi:10.1029/2004JB003185.

Steketee, J. A. (1958), On Volterra's dislocations in a semi-infinite elastic medium, *Can. J. Phys.*, *36*, 192–205.

Turcotte, D. L., and G. Schubert (2002), *Geodynamics*, 456 pp., Cambridge Univ. Press, New York.

Wang, K., R. Wells, S. Mazzotti, R. D. Hyndman, and T. Sagiya (2003), A revised dislocation model of interseismic deformation of the Cascadia subduction zone, *J. Geophys. Res.*, *108*(B1), 2026, doi:10.1029/2001JB001227.

Zoback, M. D., et al. (1987), New evidence on the state of stress of the San Andreas fault system, *Science*, *238*(4830), 1105–1111.

K. Luttrell and D. Sandwell, Scripps Institution of Oceanography, La Jolla, CA 92037, USA. (kluttrell@ucsd.edu)